Tailoring Spin Angular Momentum of Light: Design Principles for Plasmonic Nanostructures

Wen Xiao,[†] Yudong Chen,[†] Kui Han, Xiaopeng Shen, and Weihua Wang[*]
School of Physical Science and Technology, China University of Mining and Technology, Xuzhou 221116, China

(Received 19 July 2019; revised manuscript received 27 November 2019; published 16 January 2020)

Spin angular momentum (SAM), a fundamental property of light, is associated with the right-hand and left-hand circular polarizations. It has never been trivial to engineer a light beam with desired SAM, and especially at the frequency regime other than the visible region. A widely used approach is to build periodic arrays of plasmonic nanostructures that host two orthogonal dipole resonances. As the unit cell, its structure design is crucial, but the design principle remains obscure. We present a model of two orthogonal resonant Lorentz dipoles to quantitatively describe the creation of SAM in such plasmonic quarter-wave plates. The equal amplitude and $\pi/2$ phase difference are essential. The requirements can be achieved by structure modulation and, in addition, the amplitude can be manipulated by varying the polarization angle of incident waves. In practice, the resonant frequency difference of two dipoles $\Delta\omega = |\omega_A - \omega_B|$, and their damping rate κ_A and κ_B, should meet a basic criterion, such as $\Delta\omega \geqslant \sqrt{\kappa_A\kappa_B}$. As an illustration, we design a cross-shaped circular polarization convertor, and show its structure and incident angle optimization. We find the optimal working frequency ω_{opt} is roughly equal to $\sqrt{\omega_A\omega_B}$ at the critical condition $\Delta\omega = \sqrt{\kappa_A\kappa_B}$. Our results provide good guidance on the design of SAM-enabled plasmonic devices for versatile applications.

DOI: 10.1103/PhysRevApplied.13.014029

I. INTRODUCTION

Spin angular momentum (SAM), also known as spin, is an intrinsic property of elementary particles [1,2]. The SAM of photons ($+\hbar$ and $-\hbar$) is the quantum-mechanical counterpart to the right-hand and left-hand circular polarizations (CPs) of light, with electromagnetic fields rotating about the wave vector [3,4]. Traditionally, in the visible region, SAM can be generated by quarter-wave plates based on birefringence [5,6]. In nanophotonics, non-Hermitian photonics with chirality [7] and topological photonics with exceptional points [8,9] are proposed to generate SAM. In metasurfaces [10,11], SAM can be produced from coherent radiation of nanoparticles or nanoantennas that are arranged in a proper manner, especially at infrared and terahertz frequencies [12–15]. In plasmonics, SAM has been demonstrated in planar periodic arrays of identical plasmonic nanostructures [16–24]. In all designs, the unit cell is a primary factor, which acts as a particle carrying local SAM that emerges from the interplay of two orthogonal resonant modes [25–31]. The plasmonic nanostructures of this kind can also be the building block for vortex beam shaping devices [32–37], for example, an Archimedes spiral architecture formed by cross-shaped metallic slots [32,34]. On the other hand, SAM plays a very important role in enhancing chiral light-matter interactions, which has already been implemented to achieve ultrasensitive sensing down to the molecular level [38–40]. In order to boost SAM-based applications, it is quite necessary to understand the design principles for plasmonic nanostructures. However, the understanding still remains at the qualitative level [26,27], and is lacking clarity and intuition.

In this paper, we propose a general theory to quantitatively describe SAM conversion on plasmonic nanostructures and provide evidence of it on cross-shaped gold nanostructures. The theory shows that nanostructures hosting two independent and orthogonally oriented dipole modes can produce ideal SAM when the two oscillating dipoles have the equal amplitude and $\pi/2$ phase difference. Both requirements can be made suitable through controlling the geometric parameter of nanostructures, and the amplitude can be further adjusted by the polarization angle of incident waves (the angle refers to the polar angle of electric field vector with respect to the x axis, see Fig. 2(a) for a schematic illustration). Moreover, we introduce a simple Lorentz model to describe the optical response of the two orthogonal dipole modes, and find that their resonant frequencies (ω_A and ω_B) and damping rates (κ_A and κ_B) are crucial for the design. Specifically, they should satisfy a basic relationship $\Delta\omega = |\omega_A - \omega_B| \geqslant \sqrt{\kappa_A\kappa_B}$. It

[*]wh.wang@outlook.com
[†]These authors contributed equally to this work.

is more appealing that these parameters are only material and structure dependent (intrinsic properties of the plasmonic nanostructures) and can be extracted directly from eigenvalue calculations. Thus, it is a very efficient method to estimate feasibility of the design and is also a very good design guide. In the case of cross-shaped nanostructures, we show linear polarization (SAM $\sigma = 0$) can be converted to left-hand circular polarization (LHCP with SAM $\sigma = -1$) at an incident polarization angle of $(0, 90^\circ)$, and converted to right-hand circular polarization (RHCP with SAM $\sigma = +1$) at an incident polarization angle of $(90^\circ, 180^\circ)$. The flexibility originates from different initial phases of the two dipoles caused by the projection of incident electric field onto their oscillating directions, which also offers a way to improve conversion efficiency at desired working frequencies. Meanwhile, the theory points out that the optimal working frequency satisfies $\omega_{\text{opt}} = \sqrt{\omega_A \omega_B}$ under the critical condition $\Delta\omega = \sqrt{\kappa_A \kappa_B}$. It should be emphasized that the theory is not limited to specific plasmonic nanostructures discussed in this paper, and can be applied to an arbitrary plasmonic nanostructure, for instance U-shaped and E-shaped nanostructures and so on [41–43].

II. THEORETICAL MODEL

The optical response of localized surface plasmons (LSPs) in metallic nanostructures is well-described in terms of a Lorentzian charge-oscillator model [44,45]. In a system of multiple oscillations, the complex polarizability $\alpha(\omega)$ is composed of the contribution from each oscillator, and the ith component can be [37,46–48]

$$\alpha_i(\omega) = \frac{3c^3\kappa_{ri}}{2\omega_i^2} \frac{1}{\omega_i^2 - \omega^2 - i\kappa_i\omega} (i = 1, 2, \ldots, N), \quad (1)$$

where ω_i denotes the resonant frequency, κ_i is its total damping rate, and κ_{ri} is the radiative part of κ_i. These three parameters can be extracted from eigenvalue calculations. In practice, we proceed with a commercial software COMSOL MULTIPHYSICS and implement Eigenfrequency modelling in the RF Module. The computed eigenvalues are complex, which can be written as $\tilde{\Omega} = \Omega_r + i\Omega_i$. Meanwhile, the zero denominator of Eq. (1) leads to the complex resonant frequencies as well. In short, we can substitute ω with $\tilde{\Omega}$ in the denominator, and finally obtain $\omega_i = \sqrt{\Omega_r^2 + \Omega_i^2}$ and $\kappa_i = -2\Omega_i$. The last parameter κ_{ri} can be extracted similarly by setting the material with zero loss.

An incident wave with polarization angle θ, the electric field being $\mathbf{E}_{\text{inc}} = E_0(\cos\theta \mathbf{e}_x + \sin\theta \mathbf{e}_y)$, will excite those dipole modes that are not exactly orthogonal to $\mathbf{E}_{\text{inc}}$, and the net dipole moment can be readily written as

$$\mathbf{p}_{\text{net}} = \sum_{i=1}^{N} \mathbf{p}_i = \sum_{i=1}^{N} \alpha_i(\mathbf{E}_{\text{inc}} \cdot \mathbf{e}_i)\mathbf{e}_i. \quad (2)$$

For plasmonic nanostructures at optical frequencies, only the two lowest-order dipole modes, denoted as $\mathbf{p}_A$ and $\mathbf{p}_B$, are of interest [$N = 2$ in Eq. (2)]. In the absence of rotational symmetry, $\mathbf{p}_A$ and $\mathbf{p}_B$ are orthogonally oriented and nondegenerate, for example, $\mathbf{e}_A = \mathbf{e}_x$ and $\mathbf{e}_B = \mathbf{e}_y$, and $\omega_A \neq \omega_B$. In this sense, we have $\mathbf{p}_A = p_x\mathbf{e}_x$ and $\mathbf{p}_B = p_y\mathbf{e}_y$. Owing to the principle of superposition, they are able to produce coherent radiation with LHCP or RHCP when they have the equal amplitude and $\pi/2$ phase difference. Based on amplitude-phase description, they can be expressed as $\mathbf{p}_A = |\mathbf{p}_A| \exp(i\phi_A)\,\mathbf{e}_A$ and $\mathbf{p}_B = |\mathbf{p}_B| \exp(i\phi_B)\,\mathbf{e}_B$, and their ratio $\mathbf{p}_A/\mathbf{p}_B = |\mathbf{p}_A| / |\mathbf{p}_B| \exp[i(\phi_A - \phi_B)]$. The equal amplitude indicates $|\mathbf{p}_A| / |\mathbf{p}_B| = 1$, and the phase requirement means $\Delta\phi = \phi_A - \phi_B = \pi/2$. By examining Eq. (2), it is easy to find that the amplitude is not solely determined by the dipole modes, and can be further tuned by the polarization angle of incident waves (see the term $\mathbf{E}_{\text{inc}} \cdot \mathbf{e}_i$). However, the projection of incident electric field is either parallel or antiparallel to the dipole modes, which introduces a constant additional phase π in some situations. Thus, the phase difference can be separated into two parts $\Delta\phi = (\varphi_A - \varphi_B) + \Delta\varphi_0$, where $(\varphi_A - \varphi_B)$ comes from the two modes, and $\Delta\varphi_0$ is the additional phase. In our designs, $\Delta\varphi_0 = 0$ is the polarization angle at the first and third quadrant, while $\Delta\varphi_0 = \pi$ is the polarization angle at the second and fourth quadrant. Then the phase requirement can be reduced to $\Delta\varphi = \varphi_A - \varphi_B = \pi/2$, which guides the way to structure design, and the values of $\Delta\varphi_0$ only result in the radiation with either LHCP or RHCP.

The condition $\Delta\varphi = \pi/2$ can be achieved by designing the two orthogonally oriented dipole modes $\mathbf{p}_A$ and $\mathbf{p}_B$. For simplicity, we consider the polarization angle of incident waves to be 45°, which gives $\mathbf{E}_{\text{inc}} \cdot \mathbf{e}_A = \mathbf{E}_{\text{inc}} \cdot \mathbf{e}_B$. Thereby, we can investigate α_A and α_B as an alternative, whose amplitude and phase can be easily calculated from Eq. (1). Supposing their resonance frequencies $\omega_A < \omega_B$, the results are shown in Fig. 1. We find that their amplitude curves always have a point of intersection located at the frequency range $[\omega_A, \omega_B]$ (defined as the working frequency range), which corresponds to the frequency of equal amplitude, and as discussed previously, its exact position can be tuned by varying the polarization angle. However, it is not so obvious to obtain $\pi/2$ phase difference from their phase curves. As the same response line shape, the curve of φ_B is blue shifted from that of φ_A. Although the phase difference is a function of frequency, the maximum phase difference can be continuously tuned from 0 to nearly π by increasing blue shift. Thus, $\pi/2$ phase difference at the working frequency range will require the blue shift to exceed a critical value when the maximum phase difference of two curves attain $\pi/2$. It is unlikely to extract the value from Fig. 1(b), and hence a quantitative understanding should be carried forward. Starting from the ratio

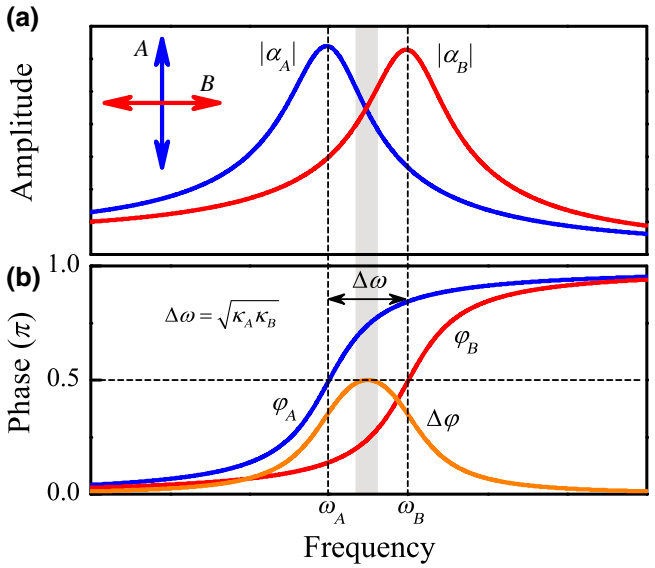

FIG. 1. The spectrum curves of two orthogonally oriented dipole resonances. (a) The amplitude spectra of mode A (blue line) and mode B (red line) with different resonant frequencies ω_A and ω_B respectively and (b), the corresponding phase response of the two modes.

$\alpha_A/\alpha_B = |\alpha_A|/|\alpha_B| \exp[i\Delta\varphi]$, when $\Delta\varphi = \pi/2$, it is a pure imaginary number with vanishing real part that gives

$$\mathbf{Re}\left(\frac{\omega_A^2 - \omega^2 - i\kappa_A\omega}{\omega_B^2 - \omega^2 - i\kappa_B\omega}\right) = 0. \tag{3}$$

After some simple algebra, Eq. (3) can be simplified to

$$\omega^4 - (\omega_A^2 + \omega_B^2 - \kappa_A\kappa_B)\omega^2 + \omega_A^2\omega_B^2 = 0. \tag{4}$$

The condition for existence of solutions is that the discriminant of the equation should be greater than or equal to zero, which is

$$(\omega_A^2 + \omega_B^2 - \kappa_A\kappa_B)^2 - 4\omega_A^2\omega_B^2 \geqslant 0. \tag{5}$$

Finally, we have

$$\Delta\omega = |\omega_A - \omega_B| \geqslant \sqrt{\kappa_A\kappa_B}. \tag{6}$$

When $\Delta\omega = \sqrt{\kappa_A\kappa_B}$, the maximum value of phase difference is $\pi/2$ [see the $\Delta\varphi$ curve, origin one in Fig. 1(b)] and, therefore, the frequency at the peak position can satisfy $\Delta\varphi = \pi/2$. When $\Delta\omega > \sqrt{\kappa_A\kappa_B}$, the peak of $\Delta\varphi$ curve will go over $\pi/2$. The $\pi/2$ phase difference can be achieved at two frequencies, which are located at the slope symmetrically with respect to the peak position. However, it is easy to find that their ways of achieving $\Delta\varphi = \pi/2$ are different. The phase difference $\Delta\varphi$ goes through $\pi/2$ smoothly at the peak, yet very rapidly at the slope. This will cause distinct consequences. If we weaken the requirement, such as $|\Delta\varphi - \pi/2| \leq 5°$, the working frequency at the peak position will have a much larger bandwidth than that at the slope. Thus, it is very interesting that the critical condition $\Delta\omega = \sqrt{\kappa_A\kappa_B}$ corresponds to the optimal working frequency, which is $\omega_{\text{opt}} = \sqrt{\omega_A\omega_B}$ as obtained by solving Eq. (4).

In order to characterize the achievement of SAM quantitatively, we introduce ellipticity χ, synthesizing the amplitude and phase, which is defined as

$$\chi = \frac{2I_AI_B\sin(\Delta\phi)}{I_A^2 + I_B^2}. \tag{7}$$

Here I_A and I_B are the intensities of radiated waves generated by the dipole modes A and B, respectively, which are linearly proportional to the square of the dipole moment, such as $I_A \propto |\mathbf{p}_A|^2$ and $I_B \propto |\mathbf{p}_B|^2$. It can be seen that χ depends on both amplitude and phase difference, but its sign depends only on the phase difference. The value of χ lies between -1 and 1, for instance $|\chi| \leqslant 1$, where the minimum (-1) and the maximum (1) represent perfect LHCP and RHCP. The condition for χ to attain the boundary values ± 1 is $|\mathbf{p}_A| = |\mathbf{p}_B|$ and $\Delta\phi = \pm\pi/2$. Another special case is $\chi = 0$ corresponding to linear polarization, which is encountered as either one of $|\mathbf{p}_A|$ and $|\mathbf{p}_B|$ being zero or $\Delta\phi = 0$. Thus, the ellipticity χ provides an efficient manner to depict SAM conversion. Even more importantly, it automatically embraces the two requirements: equal amplitude and $\pi/2$ phase difference.

We now introduce a few numerical tips for calculating the ellipticity χ. The key step is to calculate the two dipole moments $\mathbf{p}_A$ and $\mathbf{p}_B$, which can be computed from the theoretical model [Eqs. (1) and (2)] and full-wave simulations. The simulations are carried out in COMSOL MULTIPHYSICS, in which they are expressed as a surface integral involving surface charge density $\eta = \varepsilon_0 E_z$, for example $p_x = \varepsilon_0 \iint E_z x\, ds$. To verify the theory, we also compute absorption cross section σ^{abs} from the model, where $\sigma^{\text{abs}} = (\omega/c)\text{Im}\{p_x + p_y\}/E_0$, and from the simulations, in which σ^{abs} can be computed from the volume integral of a built-in function *emw.Qh* normalized by the intensity of incident waves.

III. RESULTS AND DISCUSSIONS

In order to confirm our prediction and understand the physical mechanism intensively, we employ the theory to design a SAM convertor based on cross-shaped plasmonic nanostructures, and to direct us towards the optimization procedure. Figure 2(a) shows a schematic diagram of SAM conversion ($\sigma = \pm 1$) when linearly polarized waves with polarization angle 45° and −45° incident on a cross-shaped plasmonic nanostructure. It is clear that different $\Delta\varphi_0$ leads to the radiation with different handedness. In practice, the structure is designed with two orthogonal arms

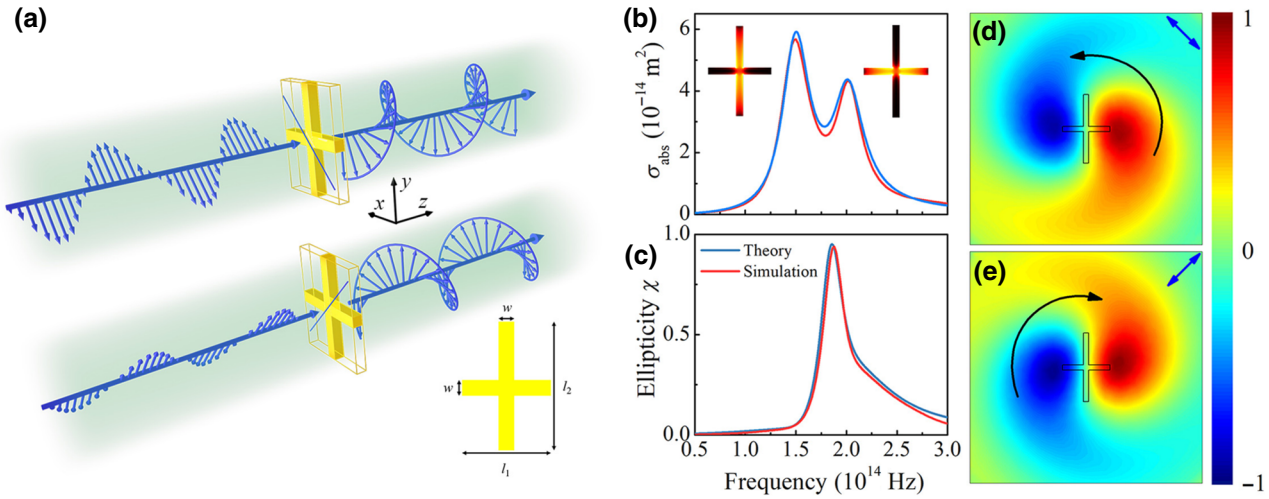

FIG. 2. (a) The schematic diagram of LHCP and RHCP conversion from linear polarization on cross-shaped plasmonic nanostructures. The illustration in the bottom right corner shows its front side, two arms of length l_1 and l_2, and with a square cross section of side length w. (b) The absorption spectra computed from theory (blue curve) and full-wave simulations (red curve) at $l_1 = 450$ nm, $l_2 = 650$ nm, and $w = 50$ nm. The insets are the surface currents (the lighter color indicates higher current density) of two resonant dipole modes at the peak positions. (c) The ellipticity χ as a function of frequency obtained from the theory (blue curve) and the simulation (red curve). The maximum value of χ leads to the best conversion efficiency. (d), (e) The normal electric field (E_z) distributions near the lateral surface (xy plane) in one moment. The patterns are rotating over time, and the arrows of each black curve give their rotational directions. The blue double-headed arrows represent the polarization direction of incident electric fields.

of same square cross section [its side length w as shown in Fig. 2(a)] and of different length [i.e., l_1 in x direction and l_2 in y direction as shown in Fig. 2(a)], which initialize different resonance frequencies for the dipole modes along two arms. In principle, the structure can be made of any noble metals. As usual, gold is chosen for the purpose, the optical response of which such as permittivity $\varepsilon(\omega)$ in the far-infrared regime can be described by a Drude model $\varepsilon(\omega) = \varepsilon_\infty - \omega_p^2/[\omega(\omega + i\gamma)]$, where $\varepsilon_\infty = 9$ is the background screening, $\omega_p = 1.37 \times 10^{16}$ rad/s is the bulk plasmon frequency, and $\gamma = 7.6 \times 10^{13}$ rad/s is the damping rate.

For an intuitive demonstration, we set the length $l_1 = 450$ nm, $l_2 = 650$ nm, and the width $w = 50$ nm. When linearly polarized light of polarization angle 45° is incident, the absorption cross sections obtained from full-wave simulation (red curve) and the theoretical model (blue curve) are shown in Fig. 2(b), where the results are in good agreement. The two peaks in the spectra are from the dipole modes along two arms, and their current distribution are indicated in the two insets. It is obvious that the current of lower-frequency mode flows in the longer arm, and that of higher-frequency mode flows in the shorter arm. Thus, their resonance frequencies can be tuned independently by the length of two arms. In Fig. 2(c), we present the ellipticity spectra obtained from simulation (red curve) and the model (blue curve). It can be seen that the perfect CP can be nearly achieved at the peak position, where the working frequency is 1.87×10^{14} Hz and the model predicts a maximum value of 0.94 for the ellipticity χ. In this case, the LHCP is shaped and its normal component of electric field (E_z field) at the surface is shown in Fig. 2(d). Similarly, if the polarization angle of the incident wave is −45°, the perfect RHCP will be roughly achieved and χ will reach −0.94 at the same working frequency. Its E_z field at the surface is shown in Fig. 2(e), which shows a different chirality with respect to the wave vector.

So far we have demonstrated the conversion of CP in cross-shaped plasmonic nanostructures. However, there are still two issues remaining: first, whether the maximum value of χ can be improved further; and, second, whether the working frequency can be tuned continuously. As indicated by the theory, these issues are closely related to the difference of resonance frequencies $\Delta\omega$. In other words, we have to manipulate the resonance frequencies of two dipole modes. As they are determined by the length of two arms separately, we can fix the length of one arm and change the length of another arm. In practice, we set $l_1 = 450$ nm, and vary the length of l_2 from 460 to 850 nm. Without loss of generality, we compute the ellipticity χ at the polarization angle of 30°. The results from theoretical model [see Fig. 3(a)] show good agreement with those from simulations [see Fig. 3(b)]. We can see that the ellipticity χ can reach its maximum value of 1 when $l_2 = 560$ nm at 1.84×10^{14} Hz, and the working frequency is not single-valued. The working frequency region, for example, the curved area for $\chi > 0.9$, exhibits an obvious red shift as an increase of l_2. Beyond this region, χ is very

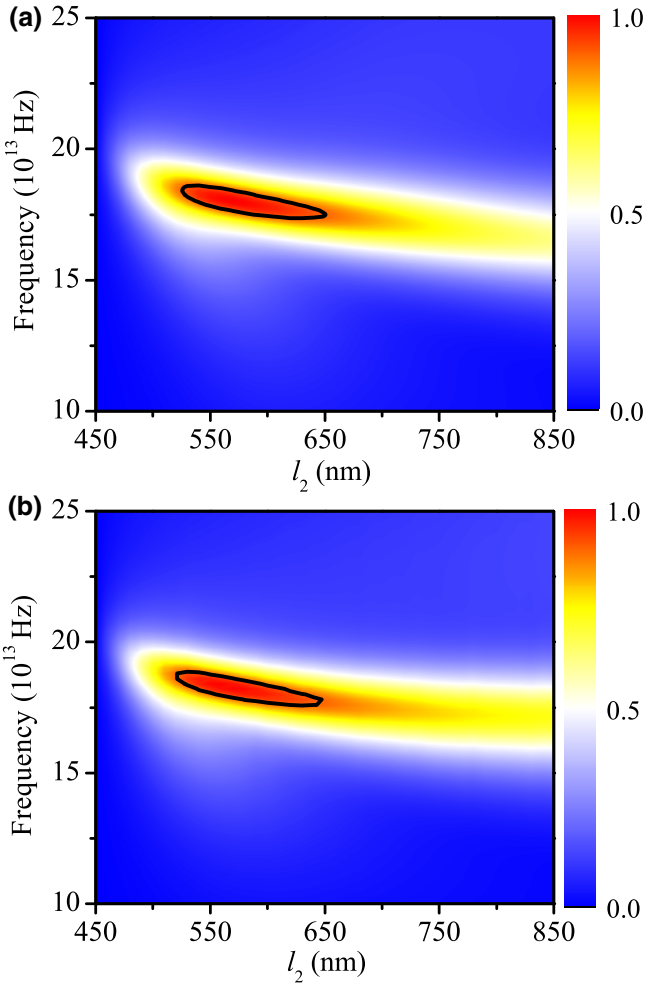

FIG. 3. The evolution of ellipticity χ as the length l_2 varies from 450 to 850 nm, on the cross-shaped plasmonic nanostructure of $l_1 = 450$ nm and $w = 50$ nm. Color maps show the results extracted from the theory (a) and from simulations (b). The black curves mark the region of $\chi \geqslant 0.9$. The same identification will be used in the following figures.

small, where the CP cannot be well produced. We note that as $l_2 < 500$ nm, χ decreases to zero rapidly. This can be easily explained by the theory, where as l_2 approaches l_1, the difference of two resonance frequencies $\Delta\omega$ becomes very small and eventually smaller than $\sqrt{\kappa_A \kappa_B}$. Owing to the theory, as $\Delta\omega < \sqrt{\kappa_A \kappa_B}$, the phase difference $\Delta\varphi$ can never achieve $\pi/2$ and even gets very close to zero. On the other side, as l_2 moves far away from l_1, χ decreases gradually. Although in this region the $\pi/2$ phase difference can be easily attained, it is very hard to meet the equal amplitude requirement at identical frequencies. As illustrated by the theory, this can be improved by choosing a better polarization angle than 30°, which is discussed in the following. We also note that there is a slight difference between Figs. 3(a) and 3(b) in this region, because for a longer l_2 the higher-order modes will get involved, which are taken into account by the full-wave simulations but not by the theory.

In such cross-shaped plasmonic nanostructures, the length of l_1 and l_2 determines both the phase difference and amplitude. In the case described previously, if we want to achieve a perfect CP at $l_2 > 750$ nm, one can increase the length of l_1 simultaneously, and the resulting working frequency will shift to a lower-frequency range. Fortunately, the amplitude can be further tuned by the polarization angle, which thereby offers an alternative way to achieve a perfect CP at $l_2 > 750$ nm. Following previous discussions, we are going to show the polarization angle optimization procedure, for instance investigating the evolution of χ at $l_2 = 500$, 560, 650, and 750 nm. The simulation results are shown in Fig. 4. It is clear that the perfect CP can never be achieved at $l_2 = 500$ nm [see Fig. 4(a)], which, as mentioned previously, stems from the absence of required phase difference. As l_2 exceeds 500 nm, the phase requirement can be satisfied, and thus the perfect CP can be obtained for certain polarization angles. However, the ellipticity χ exhibits different distributions. We find $l_2 = 560$ nm gives the best CP conversion efficiency [see Fig. 4(b), the curved area for $\chi > 0.9$], in which the working frequency can be controlled in a continuous manner. Owing to the theory, it should correspond to the case satisfying the critical condition $\Delta\omega = \sqrt{\kappa_A \kappa_B}$, and therefore the optimal working frequency $\omega_{\text{opt}} = \sqrt{\omega_A \omega_B} = 1.85 \times 10^{14}$ Hz ($\omega_A = 2.00 \times 10^{14}$ Hz at $l_1 = 450$ nm and $\omega_B = 1.72 \times 10^{14}$ Hz at $l_2 = 560$ nm), which is in a good coincidence with the optimal working frequency 1.84×10^{14} Hz extracted from the calculations. As increasing l_2 further, for instance $l_2 = 650$ nm and 750 nm as shown in Figs. 4(c) and 4(d) respectively, the continuous curved area is reduced to two separated and small parts. It means the CP conversion can only be operated in a very narrow frequency band. This might hamper its practical applications. We should emphasize that a different length of l_1 corresponds to a different optimal length of l_2. Here, the optimal length 560 nm of l_2 only works for the case of $l_1 = 450$ nm. A proper scaling law is expected in the structure design, because the wavelength of two dipole resonances is approximately equal to twice the length of each arm. Therefore, it is alternative to broaden the operating frequencies further by a simple size scaling of the structures, which could remedy the limitation of frequency bandwidth.

In order to get a better view, we extract the maximum value of χ at every polarization angle and their corresponding frequencies. The results are summarized and presented in Figs. 4(e) and 4(f). We can see that except for the curve of $l_2 = 500$ nm [red triangles in Fig. 4(e)], the other three curves can reach about 1 at certain angles. We note that the curve of $l_2 = 560$ nm [green dots in Fig. 4(e)] possesses a flat plateau, where the perfect CP conversion can be achieved in a broad angle region. Owing to our

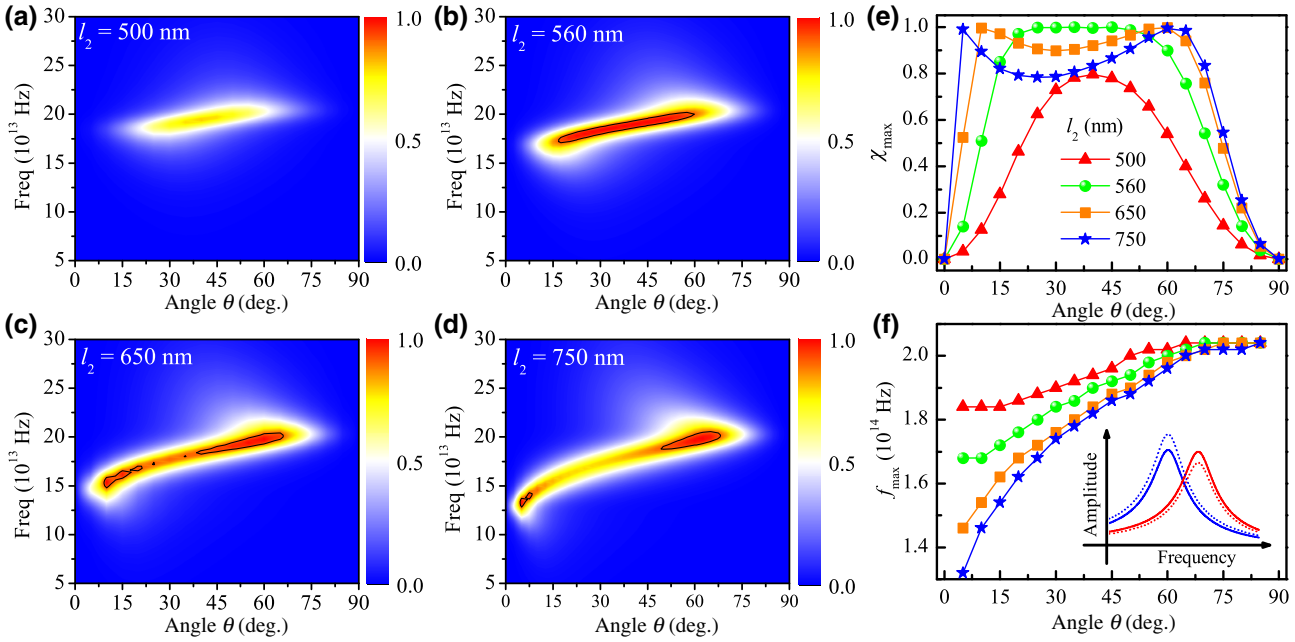

FIG. 4. The simulated ellipticity spectra as a function of the polarization angle θ (the angle between incident electric field and the shorter arm l_1) at l_2 length of (a) 500 nm, (b) 560 nm, (c) 650 nm, and (d) 750 nm. (e) The extracted maximum ellipticity χ_{max} and (f) its corresponding frequency f_{max}. In all calculations, $l_1 = 450$ nm and $w = 50$ nm. The inset in (f) shows the amplitude spectra (solid curves) of two dipole modes and their revised amplitude spectra (dashed curves) after the increase of angle θ.

calculations, the angle broadening $\Delta\theta$ can be as large as 35° and, meanwhile, the working frequency broadening Δf can be up to 3.6×10^{13} Hz. It is also very interesting that as shown in Fig. 4(f), the frequency at the maximum ellipticity gradually increases with increasing polarization angle θ. This behavior can be well explained by our theory. Referring to Fig. 1(a), the crossing point of two curves gives the frequency that meets the equal amplitude requirement. As increasing the polarization angle θ, the projection of incident electric field into x and y direction is reduced and amplified, respectively, and then the amplitude of the two dipole modes $\mathbf{p}_A$ (in x direction) and $\mathbf{p}_B$ (in y direction) will change accordingly. As illustrated by the inset in Fig. 4(f), the dashed curves represent the new amplitude responses after increasing θ. We can see that the crossing point exhibits an obvious blue shift, which is clear evidence of the discussed behavior. Here, the polarization angle dependence is quite different from that in traditional quarter-wave plates in which all frequencies should be operated at an angle of 45°. Therefore, it serves as a new degree of freedom and can be implemented to select operating frequencies, which could be useful for sensing of particular chiral materials.

It is no doubt that the proposed theory provides an efficient and easy-to-use guide for structure design. As one of the experimental works, Black and coworkers demonstrated a coupled dimer structure that can realize the CP conversion by a plane wave illumination [26]. In their work, the key point was to seek the working frequency of maximum efficiency, which is proceeded by carefully varying the distance between two orthogonally placed nanorods. Through eigenvalue calculation of their structure with $L = 230$ nm and a 13 nm gap (a simple Drude model is used here), we obtain $\omega_A = 2.21 \times 10^{14}$ Hz, $\omega_B = 2.92 \times 10^{14}$ Hz, and $\sqrt{\kappa_A \kappa_B} = 0.68 \times 10^{14}$ Hz. It is easy to find that the ratio $\Delta\omega/\sqrt{\kappa_A \kappa_B}$ is approximately equal to 1 (exactly 1.04) and the optimal working frequency $\omega_{opt} = \sqrt{\omega_A \omega_B} = 2.54 \times 10^{14}$ Hz, which is very close to the frequency 2.61×10^{14} Hz (1.15 μm wavelength) given by the experiment. Here we see a deviation from the experimental data, which comes from the Drude dielectric function especially the damping rate not being able to describe the optical response of the structure very well under experimental conditions.

IV. CONCLUSIONS

To summarize, we propose a general theory of SAM conversion on plasmonic nanostructures, in which the optical response is featured by two orthogonally oriented dipole resonances. To achieve an efficient CP conversion, they should carry the equal amplitude and $\pi/2$ phase difference. The two requirements can be realized through structural modulation and tuning the polarization angle. By introducing a simple Lorentz model to describe the two dipole modes, we find their resonant frequencies (ω_A and ω_B) and damping rates (κ_A and κ_B) should meet a basic criterion, to say $\Delta\omega = |\omega_A - \omega_B| \geqslant \sqrt{\kappa_A \kappa_B}$. These

parameters are intrinsic quantities of the structures with a given material such as gold and silver, and thus they can be extracted directly from eigenvalue calculations. Moreover, we demonstrate that the optimal working frequency is roughly given by $\omega_{\text{opt}} = \sqrt{\omega_A \omega_B}$, which can be achieved at the critical condition $\Delta\omega = \sqrt{\kappa_A \kappa_B}$. We should emphasize that the critical condition is universally applicable as far as the Lorentz model can capture the optical response of the nanostructures. As a practical case, we investigate the ellipticity χ (a quantitative parameter of CP conversion efficiency, $|\chi| \leqslant 1$) on cross-shaped gold nanostructures intensively, where the length of each arm determines the resonant frequencies of two dipole modes, and their amplitudes can be further manipulated by the polarization angle. We show that the results obtained from the theory are in good agreement with those from full-wave simulations, and perfect CP conversion ($\chi = \pm 1$) can be achieved at the optimal working frequency that is very close to $\sqrt{\omega_A \omega_B}$. Our theory provides very constructive design principles for plasmonic nanostructures that are aimed to tailor spin angular momentum and, in practice, it could be of great interest to future device applications such as plasmonic quarter-wave plates at infrared and terahertz frequencies.

ACKNOWLEDGMENTS

This work is supported by the National Natural Science Foundation of China (NSFC) (Grant No. 11604382 and Grant No. 11574140) and the Natural Science Foundation of Jiangsu Province (Grant No. BK20160236).

[1] M. Born and E. Wolf, *Principles of Optics* (Cambridge University Press, Cambridge, England, 1999), 7th ed.

[2] D. O'Connor, P. Ginzburg, F. J. Rodríguez-Fortuño, G. A. Wurtz, and A. V. Zayats, Spin–orbit coupling in surface plasmon scattering by nanostructures, Nat. Commun. **5**, 5327 (2014).

[3] X. Yin, Z. Ye, J. Rho, Y. Wang, and X. Zhang, Photonic spin hall effect at metasurfaces, Science **339**, 1405 (2013).

[4] K. Y. Bliokh, F. J. Rodríguez-Fortuño, F. Nori, and A. V. Zayats, Spin–orbit interactions of light, Nat. Photon. **9**, 796 (2015).

[5] Q. Xu, B. Schmidt, S. Pradhan, and M. Lipson, Mircometre-scale silicon electro-optic modulator, Nature **435**, 325 (2005).

[6] H. Yang, H. Jussila, A. Autere, H. P. Komsa, G. Ye, X. Chen, T. Hasan, and Z. Sun, Optical waveplates based on birefringence of anisotropic two-dimensional layered materials, ACS Photonics **4**, 3023 (2007).

[7] S. Yu, X. Piao, and N. Park, Chirality in non-hermitian photonics, Curr. Opt. Photonics **3**, 275 (2019).

[8] M. Lawrence, N. Xu, X. Zhang, L. Cong, J. Han, W. Zhang, and S. Zhang, Manifestation of PT Symmetry Breaking in Polarization Space with Terahertz Metasurfaces, Phys. Rev. Lett. **113**, 093901 (2014).

[9] S. Yu, H. S. Park, X. Piao, B. Min, and N. Park, Low-dimensional optical chirality in complex potentials, Optica **3**, 1025 (2016).

[10] N. Yu, P. Genevet, M. A. Kats, F. Aieta, J. P. Tetienne, F. Capasso, and Z. Gaburro, Light propagation with phase discontinuities: Generalized laws of reflection and refraction, Science **334**, 333 (2011).

[11] S. Sun, Q. He, S. Xiao, Q. Xu, X. Li, and L. Zhou, Gradient-index meta-surfaces as a bridge linking propagating waves and surface waves, Nat. Mat. **11**, 426 (2012).

[12] N. Yu, F. Aieta, P. Genevet, M. A. Kats, Z. Gaburro, and F. Capasso, A broadband, background-free quarter-wave plate based on plasmonic metasurfaces, Nano Lett. **12**, 6328 (2012).

[13] L. Cong, N. Xu, J. Gu, R. Singh, J. Han, and W. Zhang, Highly flexible broadband terahertz metamaterial quarter-wave plate, Laser Photonics Rev. **8**, 626 (2014).

[14] D. Wang, L. Zhang, Y. Gu, M. Q. Mehmood, Y. Gong, A. Srivastava, L. Jian, T. Venkatesan, C.-W. Qiu, and M. Hong, Switchable ultrathin quarter-wave plate in terahertz using active phase-change metasurface, Sci. Rep. **5**, 15020 (2015).

[15] S.-C. Jiang, X. Xiong, Y.-S. Hu, S.-W. Jiang, Y.-H. Hu, D.-H. Xu, R.-W. Peng, and M. Wang, High-efficiency generation of circularly polarized light via symmetry-induced anomalous reflection, Phys. Rev. B **91**, 125421 (2015).

[16] S.-C. Jiang, X. Xiong, Y.-S. Hu, Y.-H. Hu, G.-B. Ma, R.-W. Peng, C. Sun, and M. Wang, Controlling the Polarization State of Light with a Dispersion-Free Metastructure, Phys. Rev. X **4**, 021026 (2014).

[17] D. Wang, Y. Gu, Y. Gong, C.-W. Qiu, and M. Hong, An ultrathin terahertz quarter-wave plate using planar babinet-inverted metasurface, Opt. Express **23**, 11114 (2015).

[18] W. Ye, X. Yuan, C. Guo, J. Zhang, B. Yang, and S. Zhang, Large Chiroptical Effects in Planar Chiral Metamaterials, Phys. Rev. Appl. **7**, 054003 (2017).

[19] Y. Zhao and A. Alù, Tailoring the dispersion of plasmonic nanorods to realize broadband optical meta-wave plates, Nano Lett. **13**, 1086 (2013).

[20] N. K. Grady, J. E. Heyes, D. R. Chowdhury, Y. Zeng, M. T. Reiten, A. K. Azad, A. J. Taylor, D. A. R. Dalvit, and H.-T. Chen, Terahertz metamaterials for linear polarization conversion and anomalous refraction, Science **340**, 1304 (2013).

[21] J. Kim, S. Choudhury, C. DeVault, Y. Zhao, A. V. Kildishev, V. M. Shalaev, A. Alù, and A. Boltasseva, Controlling the polarization state of light with plasmonic metal oxide metasurface, ACS Nano **10**, 9326 (2016).

[22] Y. Yang, W. Wang, P Moitra, I. I. Kravchenko, D. P. Briggs, and J. Valentine, Dielectric meta-reflectarray for broadband linear polarization conversion and optical vortex generation, Nano Lett. **14**, 1394 (2014).

[23] L. Huang, X. Chen, H. Mühlenbernd, G. Li, B. Bai, Q. Tan, G. Jin, T. Zentgraf, and S. Zhang, Dispersionless phase discontinuities for controlling light propagation, Nano Lett. **12**, 5750 (2012).

[24] L. Guan, Z. He, D. Ding, Y. Yu, W. Zhang, and R. Chen, Polarization-controlled shared-aperture metasurface for

generating a vortex beam with different modes, IEEE Trans. Antennas Propag. **66**, 7455 (2018).
[25] T. J. Davis, D. E. Gómez, and K. C. Vernon, Simple model for the hybridization of surface plasmon resonances in metallic nanoparticles, Nano Lett. **10**, 2618- (2010).
[26] L.-J. Black, Y. Wang, C. H. de Groot, A. Arbouet, and O. L. Muskens, Optimal polarization conversion in coupled dimer plasmonic nanoantennas for metasurfaces, ACS Nano **8**, 6390 (2014).
[27] P. R. Wiecha, L.-J. Black, Y. Wang, V. Paillard, C. Girard, O. L. Muskens, and A. Arbouet, Polarization conversion in plasmonic nanoantennas for metasurfaces using structural asymmetry and mode hybridization, Sci. Rep. **7**, 409067 (2017).
[28] N. Meinzer, W. L. Barnes, and I. R. Hooper, Plasmonic meta-atoms and metasurfaces, Nat. Photon. **8**, 889 (2014).
[29] J. Sung, M. Sukharev, E. M. Hicks, R. P. Van Duyne, T. Seideman, and K. G. Spears, Nanoparticle spectroscopy: Birefringence in two-dimensional arrays of L-shaped silver nanoparticles, J. Phys. Chem. C **112**, 3252 (2008).
[30] P. Biagioni, M. Savoini, J.-S. Huang, L. Duò, M. Finazzi, and B. Hecht, Near-field polarization shaping by a near-resonant plasmonic cross antenna, Phys. Rev. B **80**, 153409 (2009).
[31] J. Zuloaga and P. Nordlander, On the energy shift between near-field and far-field peak intensities in localized plasmon systems, Nano Lett. **11**, 1280 (2011).
[32] C.-F. Chen, C.-T. Ku, Y.-H. Tai, P.-K. Wei, H.-N. Lin, and C.-B. Huang, Creating optical near-field orbital angular momentum in a gold metasurface, Nano Lett. **15**, 2746 (2015).
[33] H. Wang, L. Liu, C. Liu, X. Li, S. Wang, Q. Xu, and S. Teng, Plasmonic vortex generator without polarization dependence, New J. Phys. **20**, 033024 (2018).
[34] H. Yang, Y. Deng, G. Cao, J. Chen, J. Li, and W. Sun, Switching the topological charge of surface plasmon vortex by tailoring polarization states, IEEE Photon. Tech. Lett. **29**, 1784 (2017).
[35] Q. Tan, Q. Guo, H. Liu, X. Huang, and S. Zhang, Controlling plasmonic orbital angular momentum by combining geometric and dynamic phase, Nanoscale **9**, 4944 (2017).
[36] F. Huang, X. Jiang, H. Yuan, and X. Sun, Generation of plasmonic vortex with linearly polarized light, Plasmonics **12**, 751 (2016).
[37] X. Yin, M. Schäferling, B. Metzger, and H. Giessen, Interpreting chiral nanophotonic spectra: The plasmonic born-kuhn model, Nano Lett. **13**, 6238 (2013).
[38] Y. Zhao, A. N. Askarpour, L. Sun, J. Shi, X. Li, and A. Alù, Chirality detection of enantiomers using twisted optical metamaterials, Nature Commun. **8**, 14180 (2017).
[39] S. Lee, S. Yoo, and Q-Han Park, Microscopic origin of surface-enhanced circular dichroism, ACS Photonics **4**, 2047 (2017).
[40] S. Yoo and Q-Han Park, Metamaterials and chiral sensing: A review of fundamentals and applications, Nanophotinics **8**, 249 (2019).
[41] X. Huang, D. Yang, and H. Yang, Multiple-band reflective polarization converter using U-shaped metamaterial, J. Appl. Phys. **115**, 103505 (2014).
[42] H. Su, X. Shen, G. Su, L. Li, J. Ding, F. Liu, P. Zhan, Y. Liu, and Z. Wang, Efficient generation of microwave plasmonic vortices via a single deep-subwavelength meta-particle, Laser Photonics Rev. **12**, 1800010 (2018).
[43] B.-Q. Lin, J.-X. Guo, P. Chu, W.-J. Huo, Z. Xing, B.-G. Huang, and L. Wu, Multiple-Band Linear-Polarization Conversion and Circular Polarization in Reflection Mode Using a Symmetric Anisotropic Metasurface, Phys. Rev. Appl. **9**, 024038 (2018).
[44] M. Kats, P. Genevet, G. Aoust, N. Yu, R. Blanchard, F. Aieta, Z. Gaburroa, and F. Capassoa, Giant birefringence in optical antenna arrays with widely tailorable optical anisotropy, Proc. Natl. Acad. Sci. USA **109**, 12364 (2012).
[45] J. H. Choe, J. H. Kang, D. S. Kim, and Q-Han Park, Slot antenna as a bound charge oscillator, Opt. Express **20**, 6521 (2012).
[46] S. Thongrattanasiri, F. H. L. Koppens, and F. J. G. de Abajo, Complete Optical Absorption in Periodically Patterned Graphene, Phys. Rev. Lett. **108**, 047401 (2012).
[47] J. Bosse, Lorentz atom revisited by solving the abraham-lorentz equation of motion, Z. Naturforsch. A **72**, 717 (2017).
[48] N. Verellen, F. López-Tejeira, R. Paniagua-Domínguez, D. Vercruysse, D. Denkova, L. Lagae, P. V. Dorpe, V. V. Moshchalkov, and J. A. Sánchez-Gil, Mode parity-controlled fano- and lorentz-like line shapes arising in plasmonic nanorods, Nano Lett. **14**, 2322 (2014).